

Fourier domain optical tool normalization for quantitative parametric image reconstruction

Jing Qin,* Richard M. Silver, Bryan M. Barnes, Hui Zhou, and Francois Goasmat

Semiconductor and Dimensional Metrology Division, Physical Measurement Laboratory, National Institute of Standards and Technology, 100 Bureau Dr. MS 8212, Gaithersburg, Maryland 20899-8212, USA

*Corresponding author: jing.qin@nist.gov

Received 10 May 2013; accepted 16 June 2013;
posted 31 July 2013 (Doc. ID 190340); published 5 September 2013

There has been much recent work in developing advanced optical metrology methods that use imaging optics for critical dimension measurements and defect detection. Sensitivity to nanometer-scale changes has been observed when measuring critical dimensions of subwavelength 20 nm features or when imaging defects below 15 nm using angle-resolved and focus-resolved optical data. However, these methods inherently involve complex imaging optics and analysis of complicated three-dimensional electromagnetic fields. This paper develops a new approach to enable the rigorous analysis of three-dimensional, through-focus, or angle-resolved optical images. We use rigorous electromagnetic simulation with enhanced Fourier optical techniques, an approach to optical tool normalization, and statistical methods to evaluate sensitivities and uncertainties in the measurement of subwavelength three-dimensional structures. © 2013 Optical Society of America

OCIS codes: (120.3940) Metrology; (120.5820) Scattering measurements.
<http://dx.doi.org/10.1364/AO.52.006512>

1. Introduction

Success in developing advanced optical metrology methods that use imaging optics for subwavelength dimensional measurements is in part based on the analysis of the phase and scattered frequency information available when using image-based systems. For some time it has been shown that sensitivity to nanometer-scale changes can be observed when measuring dimensions of subwavelength features or when imaging small sub-20 nm patterned defects using angle-resolved and focus-resolved optical imaging [1,2]. Although there are many advantages to using low-cost high-throughput optical measurement systems, quantitative use of these methods has been limited since they inherently involve complex imaging optics and analysis of complicated three-dimensional scattered electromagnetic fields.

Previous work using optical imaging methods in a scatterfield platform to perform what are essentially angle-resolved scatterometry measurements on a high magnification imaging platform was focused on acquiring images as a function of angle for dense arrays of lines that fill the field of view (FOV) with targets similar to those used in scatterometry [3,4]. These measurements were analyzed with rigorous electromagnetic scattering and regression methods, and uncertainties were calculated. Prior to these measurements, attempts were made to model images and line profiles acquired through focus [5,6]. This required modeling the complete three-dimensional electromagnetic field as it was imaged as a function of focus position. Although robust data were acquired through focus, successful quantitative agreement between theory and experiment was not achieved. This was largely due to two primary shortcomings. First, detailed optical tool functions needed to be developed to normalize and correct for the illumination and collection optical path errors, each of which independently has a direct impact on the

1559-128X/13/266512-11\$15.00/0
© 2013 Optical Society of America

resulting experimental images. The second effect is that even in the nominally simplest single plane wave illumination example, the scattered light from any finite target has a large range of spatial frequencies that need to be accurately normalized and modeled.

Acceptable quantitative statistical analysis with rigorous agreement at the nanometer scale between experiment and theory would represent an important advance in image-based optical metrology of subwavelength features. It could provide a means for dimensional metrology of very small subfield targets. The scattered field can also result from non-repetitive and irregular structures unlike those required for scatterometry, providing important flexibility in the type of measurable structures. However, a key to the success of scatterometry has been the ability to model measurements with a high degree of accuracy and to quantitatively address parametric correlation in measurement uncertainty. This is the primary challenge in image-based optical metrology of subwavelength features.

Here we present an approach that enables the rigorous analysis of three-dimensional through-focus and angle-resolved optical images. These imaging methods sample the three-dimensional electromagnetic fields above the sample or target of interest. The technique involves parametric fitting of the discretized three-dimensional scattered field and allows for the quantitative evaluation of correlation effects due to fitting parameters such as sidewall, feature profile, and depth. Using this approach, it becomes possible to perform dimensional measurements of subwavelength features through imaging and analysis of high-order, scattered three-dimensional optical fields.

In this paper we use rigorous electromagnetic simulation, experimental data analysis, and statistical methods to evaluate sensitivities and uncertainties in the measurement of two- and three-dimensional structures. A key development presented here is the systematic correction and normalization of the scattered fields in the Fourier domain based on a comprehensive experimental set of optical “tool functions.” To facilitate rigorous measurements of the through-focus three-dimensional field data, illumination engineering and sophisticated optical path normalization are needed separately for the illumination path and the collection path. The rigorous analysis of optical imaging data then necessitates using both theoretical and experimental methods, since a nonlinear correction of the scattered electromagnetic field is required for image reconstruction.

An appropriate hardware platform that provides access to a conjugate illumination back focal plane giving full angular control of the optical path is required to facilitate acquisition of the full instrument characterization functions. We first perform a simulation study to develop the basic understanding of possible measurement sensitivities and

uncertainties. This section of the paper is intended to give a realistic evaluation of possible experimentally achievable measurement uncertainties using a realistic instrument and sample noise model. This is then followed by a full implementation of the experimental methodology to acquire three-dimensional images, and by a subsequent simulation to experiment fitting sequence and the resulting parametric uncertainties.

2. Hardware Platform and Complex Tool Normalization

The scatterfield microscopy technique, which provides full access and control of the angular distribution of the incident light, has been described in detail elsewhere [7,8]. The basic instrument is based on a Köhler illuminated bright field microscope with a large accessible conjugate back focal plane (CBFP), each point at which maps to a group of plane waves confined in 0.13 numerical aperture (NA) with specific incident angle of illumination at the sample as illustrated in Fig. 1. By scanning an aperture in the CBFP or using a fixed aperture, we can select the incident angle to realize angle-resolved characterization and measurements. Also, polarization states can be defined at the CBFP with respect to the sample and imaging optics. Data are acquired as a function of angle or focus position. A charge-coupled device (CCD) image is captured at each angle or focus position. A kernel of each image is averaged into a profile, and these are stored as arrays as a function of angle or focus position; then they are concatenated into a string data set for parametric fitting and statistical analysis. The use of a low-illumination NA with incoherent illumination is often preferred to using a large NA, because this results in better-defined and characterized illumination and reduces the loss of information from averaging in a large NA illumination system.

For finite targets, such as very small subfield targets, nonrepetitive and irregular structures that scatter multiple scattering orders, or even continuous frequency content, the normalization required to correct the experimental data for instrumentation and hardware errors becomes complex. The microscope consists of two groups of optical elements, illumination path optics and collection path optics, and multiple scattering orders propagate in the collection path optics differently from the illumination path optics. The illumination path optics determine the light

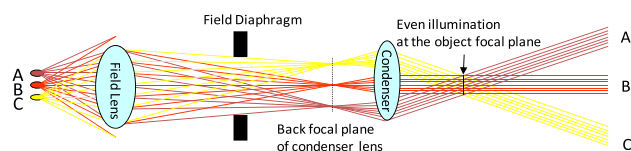


Fig. 1. Schematic for a Köhler illuminator. While the general use of Köhler illumination is to illuminate a sample homogeneously even if the source is inhomogeneous, Köhler also permits illumination engineering, such as off-axis illumination, within scatterfield microscopes.

incident on the sample, while the collection path optics affect the scattered light propagation as a function of angle and polarization. They both introduce instrumentation errors to the image. To implement accurate library-based fitting methods based on electromagnetic scattering simulations, proper experimental normalization procedures combined with rigorous modeling are needed to allow accurate comparison of angle-resolved or focus-resolved measurements with theory.

In practice, this is very complicated when the resulting high-order scattered light has scattered spatial frequencies that are continuous, and no simple method exists to isolate and measure the individual orders and normalize them separately. However, since electromagnetic scattering simulations inherently identify the scattering direction of each order, or a series of propagating plane waves can be used to represent the propagating field, we apply the collection path tool function to the amplitudes of the simulated scattered orders before the simulated image is constructed. Furthermore, the illumination path also needs to be characterized in order to correct the experimental data, as the simulations assume unit incident light at each angle and polarization. Thus, both the illumination path tool function and the collection path tool function must be calculated and implemented separately for each individual illumination angle and the resulting vast spectrum of scattered light. Stated differently, the tool must be characterized as a function of polarization and angle over the entire conjugate back plane.

The actual acquisition of the illumination tool function is accomplished by placing a photodiode (PD) detector covered by a linearly polarized analyzer at the sample plane and acquiring intensities with the analyzer aligned with the x and y axes of that plane. Similarly, a polarizer is aligned with the x and y axes of the CBFP (which corresponds to the sample plane) in the illumination path, yielding intensity results from four polarizer-analyzer combinations $I_{PD-XX}(\theta, \varphi)$, $I_{PD-XY}(\theta, \varphi)$, $I_{PD-YX}(\theta, \varphi)$, and $I_{PD-YY}(\theta, \varphi)$, which are determined experimentally using

$$\begin{aligned} & \begin{bmatrix} \sqrt{I_{PD-XX}(\theta, \varphi)} & \sqrt{I_{PD-YX}(\theta, \varphi)} \\ \sqrt{I_{PD-XY}(\theta, \varphi)} & \sqrt{I_{PD-YY}(\theta, \varphi)} \end{bmatrix} \\ &= \begin{bmatrix} -\cos \theta \cos \varphi & \sin \theta \cos \varphi \\ -\cos \theta \sin \varphi & \sin \theta \sin \varphi \end{bmatrix} \\ & \cdot \begin{bmatrix} PD_{SS}(\theta, \varphi) & 0 \\ 0 & PD_{PP}(\theta, \varphi) \end{bmatrix} \\ & \cdot \begin{bmatrix} A_{SS}(\theta, \varphi) & A_{PS}(\theta, \varphi) \\ A_{SP}(\theta, \varphi) & A_{PP}(\theta, \varphi) \end{bmatrix} \\ & \cdot \begin{bmatrix} I_{xs}(\theta, \varphi) & I_{ys}(\theta, \varphi) \\ I_{xp}(\theta, \varphi) & I_{yp}(\theta, \varphi) \end{bmatrix} \cdot \begin{bmatrix} E_x \\ E_y \end{bmatrix}. \end{aligned} \quad (1)$$

The analyzer matrix $\begin{bmatrix} A_{SS}(\theta, \varphi) & A_{PS}(\theta, \varphi) \\ A_{SP}(\theta, \varphi) & A_{PP}(\theta, \varphi) \end{bmatrix}$ is characterized on the bench top as a function of zenith angle θ and azimuth angle φ . Its four components correspond to the ss , sp , ps , and pp polarizer-analyzer combinations. The PD is also characterized on the bench as a function of angle in order to get the PD matrix $\begin{bmatrix} PD_{SS}(\theta, \varphi) & 0 \\ 0 & PD_{PP}(\theta, \varphi) \end{bmatrix}$. Then, a mirror or silicon surface is placed at the sample plane, and the intensity from these same four polarization states is acquired at the CCD image detector through the complete path, $I_{CCD-XX}(\theta, \varphi)$, $I_{CCD-XY}(\theta, \varphi)$, $I_{CCD-YX}(\theta, \varphi)$, and $I_{CCD-YY}(\theta, \varphi)$, where

$$\begin{aligned} & \begin{bmatrix} \sqrt{I_{CCD-XX}(\theta, \varphi)} & \sqrt{I_{CCD-YX}(\theta, \varphi)} \\ \sqrt{I_{CCD-XY}(\theta, \varphi)} & \sqrt{I_{CCD-YY}(\theta, \varphi)} \end{bmatrix} \\ &= \begin{bmatrix} A_{xx} & A_{yx} \\ A_{xy} & A_{yy} \end{bmatrix} \cdot \begin{bmatrix} C_{sx}(\theta, \varphi) & C_{px}(\theta, \varphi) \\ C_{sy}(\theta, \varphi) & C_{py}(\theta, \varphi) \end{bmatrix} \\ & \cdot \begin{bmatrix} R_{\text{ref-ss}}(\theta, \varphi) & R_{\text{ref-ps}}(\theta, \varphi) \\ R_{\text{ref-sp}}(\theta, \varphi) & R_{\text{ref-pp}}(\theta, \varphi) \end{bmatrix} \\ & \cdot \begin{bmatrix} I_{xs}(\theta, \varphi) & I_{ys}(\theta, \varphi) \\ I_{xp}(\theta, \varphi) & I_{yp}(\theta, \varphi) \end{bmatrix} \cdot \begin{bmatrix} E_x \\ E_y \end{bmatrix}. \end{aligned} \quad (2)$$

Here, $\begin{bmatrix} E_x \\ E_y \end{bmatrix}$ is either $\begin{bmatrix} 1 \\ 0 \end{bmatrix}$ or $\begin{bmatrix} 0 \\ 1 \end{bmatrix}$ and $\begin{bmatrix} A_{xx} & A_{yx} \\ A_{xy} & A_{yy} \end{bmatrix}$ is either $\begin{bmatrix} 1 & 0 \\ 0 & 0 \end{bmatrix}$ or $\begin{bmatrix} 0 & 0 \\ 0 & 1 \end{bmatrix}$. Through matrix calculation, we can determine the illumination path tool function, $\begin{bmatrix} I_{xs}(\theta, \varphi) & I_{ys}(\theta, \varphi) \\ I_{xp}(\theta, \varphi) & I_{yp}(\theta, \varphi) \end{bmatrix}$. The collection path tool function, $\begin{bmatrix} C_{sx}(\theta, \varphi) & C_{px}(\theta, \varphi) \\ C_{sy}(\theta, \varphi) & C_{py}(\theta, \varphi) \end{bmatrix}$, is not measured directly but is calculated using Eq. (2). An example of the tool function maps as a function of angle and polarization for the illumination path, complete path, and collection path is shown in Fig. 2. For well-defined X (or Y) polarization in the illumination optics, there are results showing partially polarized X (or Y) light that is rotated into Y (or X) polarized light for both the illumination path tool function and the complete path tool function as shown in Fig. 3. The XY or YX polarization states are due to polarization mixing from a given microscope configuration, although it should be noted that the scales on the cross terms (XY and YX) are 10^{-3} times smaller than both the illumination path and the complete path and as a result were not taken into account in the current calculation of the collection path tool function.

Once the illumination and collection path tool functions have been acquired for the entire range of angles and polarization states, normalization of the scattered field is performed in the frequency domain. The incident illumination is first independently normalized by the illumination path tool function. Then the collection path normalization is accomplished by applying the collection path tool function to the simulated scattered frequency components before the resulting simulated image is constructed at the image plane, shown schematically on the left in Fig. 3. After the image is reconstructed,

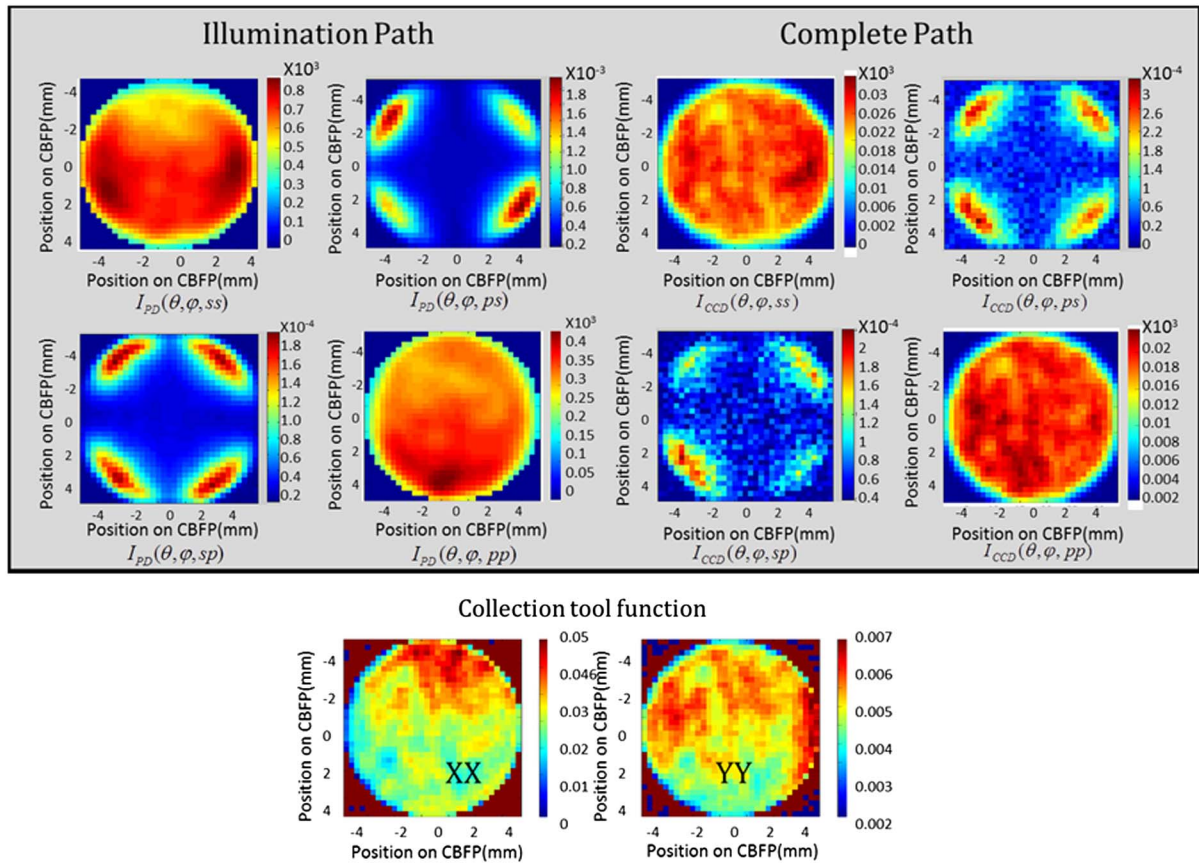


Fig. 2. Maps for the four polarizer–analyzer combinations for each point in the CBFP for the illumination path tool function and complete path function matrices. The color bars for the illumination and complete path are intensities with CCD units, and the color scales on the cross terms (XY and YX) are 10^{-3} times smaller than the scales of the other plots. The color bars for collection tool function show the transmissivity of the collection path.

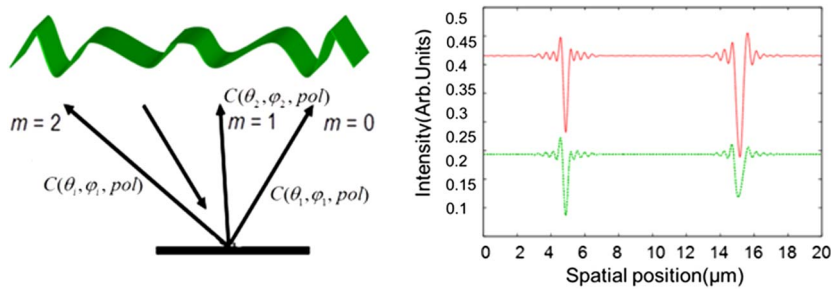


Fig. 3. Method for tool normalization when high-order scattered light is present. Both scattered light angles and polarization states need to be correctly normalized. The top curve shows uncorrected simulation data, and the one below shows the reconstructed image after Fourier normalization.

an average profile from the reconstructed image is shown as the green curve in the right plot of Fig. 3.

Great care needs to be taken to quantify and account for the off-axis behavior of the system in the case of off-axis scattered orders, and this is particularly challenging as the detectors and polarizers have nonoptimum behavior at oblique, off-axis angles of incidence.

3. Regression Analysis and Simulation Studies

We now develop a nonlinear regression model applicable to a set of images. Although the model can be

expanded using a Bayesian approach to include *a priori* information for hybrid metrology, we only employ a single measurement tool in this paper. Only an overview to the initial derivation is given here; see [9,10] for a more detailed formalism.

In general a complete set of measurements consists of N data points acquired under a varying set of conditions for both simulations and experimental measurements. The K model parameters are expressed as a vector $a = \{a_1, \dots, a_K\}$, and represent the model input parameters, for example, critical dimension (CD), sidewall, and height. We have N

measured values of Y denoted as $\{y_1, \dots, y_N\}$ and N simulated values $y(x_i; a)$ corresponding to the i th data point x_i . We want to compare the measured $\{y_1, \dots, y_N\}$ with simulated $y(x_i; a)$, $i = 1, \dots, N$ and find an optimal estimator of the parameter vector $a = \{a_1, \dots, a_K\}$. In general, $y(x_i; a)$ is a nonlinear function of a . Treating $y(x_i; a)$ as a mean response of y_i , and by using a first-order Taylor expansion, a linear approximation of the nonlinear regression for y_i is given by

$$y_i = y(x_i; a(0)) + \sum_{k=1}^K \left[\frac{\partial y(x_i; a)}{\partial a_k} \right]_{a=a(0)} (a_k - a_k(0)) + \varepsilon_i, \quad (3)$$

where $a(0) = \{a_1(0), \dots, a_K(0)\}$ is an initial value or an optimal value of a and ε_i is the corresponding random error with zero mean [11]. By reparameterization, the model can be expressed as

$$y_i = \sum_{k=1}^K D_{ik}(0) \beta_k(0) + \varepsilon_i \quad (4)$$

with $\beta_k(0) = a_k - a_k(0)$, $y_i(0) = y_i - y(x_i; a(0))$, and $D_{ik}(0) = [\partial y(x_i; a) / \partial a_k]_{a=a(0)}$. The covariance matrix of the experimental values $\{y_1, \dots, y_N\}$ is denoted by $V = \text{diag}[\sigma_1^2, \dots, \sigma_N^2]$. We can now write the reparameterized model from Eq. (4) in matrix form:

$$\mathbf{Y}(0) = \mathbf{D}(0)\boldsymbol{\beta}(0) + \boldsymbol{\varepsilon}. \quad (5)$$

It can be shown [12] that the generalized least-squares estimator of $\boldsymbol{\beta}(0)$ is now given by

$$\hat{\boldsymbol{\beta}}(0) = (\mathbf{D}(0)^T V^{-1} \mathbf{D}(0))^{-1} \mathbf{D}(0)^T V^{-1} \mathbf{Y}(0), \quad (6)$$

where $\hat{\boldsymbol{\beta}}(0) = (\hat{\beta}_1(0), \dots, \hat{\beta}_K(0))$ are the best linear unbiased estimators of $\boldsymbol{\beta}(0)$, from which we can get the best estimators of parameter \mathbf{a} . In the regression approach outlined here, we concatenate the data from each experimental image into a series of profiles resulting in one data string and solve for the best parameter fit and parametric uncertainties as we have previously outlined. Similarly, the series of images or profiles acquired as a function of focus or angle is concatenated into a data string and treated within the existing regression model.

Before applying this approach to experimental data sets, a simulation-based study was carried out to evaluate this technique for dimensional metrology of finite small dense array targets and the resulting decrease in uncertainty. We added a noise profile that contains both realistic systematic errors and random noise, shown in Fig. 4, to a simulated image that was chosen from a central location in the simulation library space. This noise-laden simulation set is then treated as the “experimental” data set to be fit. Then we concatenated all data sets from different focus positions or from different incident angles into one data string, on which the parametric fitting and a standard regression analysis are performed and uncertainty is calculated. This approach allowed us to perform a modeling comparison from the edges of a finite subfield scatterometry target (subfield dense array). The potential use of this technique for finite targets is of particular interest because it allows a baseline calibration to silicon for the nearby substrate region.

Our scattering simulation methods include a finite-difference time-domain approach and a rigorous coupled waveguide analysis (RCWA) [13], both of which were developed in house. In-house model development is critically important, as significant modification of the Fourier optical simulation components was required. Using the in-house models, Fourier domain normalization before image reconstruction becomes possible. For the simulation study of finite targets, we chose two targets with 9 nm linewidth and 32 nm pitch (L9P32) as well as with 9 nm linewidth and 160 nm pitch (L9P160), as shown in Fig. 5. On the left is shown the nominal target geometry including the CD, the number of lines, and the pitch as well as the macropitch. The macropitch is the period over which the finite grating is repeated in the numerical simulations while the lines are infinite in length for these simulations. In the center part of the figure, examples of the simulated “experimental” curves are overlaid with the best fit curves from the simulation library. On the right, the standard 1σ parametric fitting uncertainties are shown for the four floated parameters for both through-focus and angle-resolved analysis.

These data are for the L9P32 finite arrays in the upper portion, and L9P160 in the lower part of the figure. The macropitch for the simulation of these particular targets is chosen to be large enough that

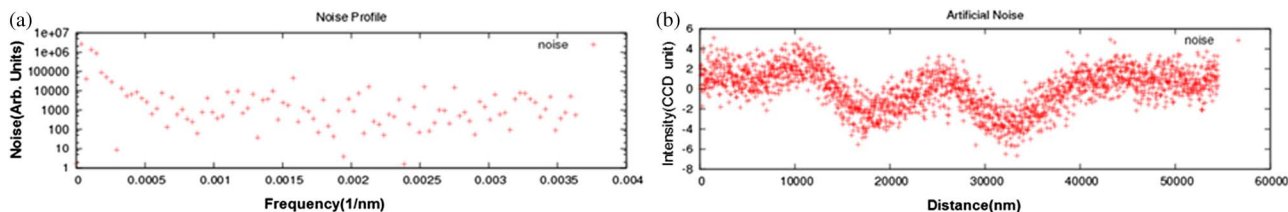


Fig. 4. (a) Realistic noise spectrum based on experimental data. (b) One example of a noise profile based on the noise spectrum from (a). This noise is added to a simulation to emulate an “experimental” curve.

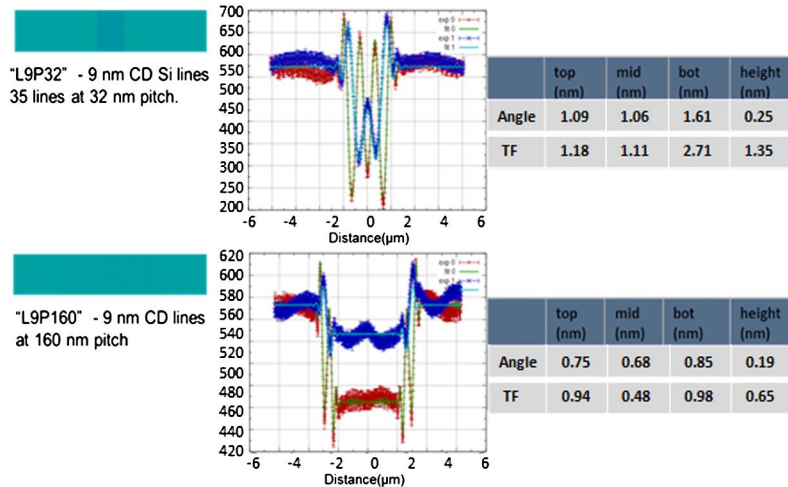


Fig. 5. Two simulation studies for finite gratings simulated using RCWA at $\lambda = 450$ nm. Each angle scan or through-focus scan consists of 84 concatenated “experimental” profiles, which are noise-added simulated images at various incident angles or focus positions. The center graphs each show the best fit simulation curves for the given “experimental” curves for two orthogonal linear polarizations (in red and blue) at a selected focus or angle position. Parametric uncertainties for both the angle-resolved and focus-resolved simulation studies at 160 nm pitch show less than 1 nm uncertainties (1σ) using this technique.

the array edges are “isolated” from interacting optically with periodic duplicates of the array, and we chose 35 lines in the array so that the central region reaches its nominal steady-state optical response as would occur in an infinite array. Phase interactions among lines near the array edge contribute to the scattered field of the edge, so that the transition between the “infinite” grating and the edge contains significant measurable information.

The uncertainties are again based on the noise profiles shown in Fig. 5 and are realistic if not overly conservative. One concern when measuring finite arrays as measured above is that the outermost edge may have an inordinately large effect on the scattered profile and potentially dominate the signal. We have investigated this possibility in simulation, and the conclusion is that the outermost edge has an effect approximately inversely proportional to the number of lines that scatter high-order light [14]. On further investigation, the data show that in the middle of a sufficiently large array, a steady-state scattered signal is achieved midarray; however, as one approaches the edge, the scattered light transitions from diffraction grating behavior to isolated feature scattering behavior with a continuum of spatial frequency information. The image content and frequency information are not dominated by the outermost features. For the L9P32 target, with only 35 lines in the array and small pitch values, steady-state specular optical response is not observed in the middle region as compared to the L9P160 target. The optical response from both edges of the target L9P32 interact with each other, resulting in interesting behavior with rich optical content in the middle region, shown in the middle of the upper portion of Fig. 5. In both the upper and lower portions of Fig. 5, subnanometer parametric

uncertainty is achieved for both targets. Although experimental validation for these finite targets has not yet been performed, the simulations here are intended to illustrate the potential application of this methodology to a new range of deep subwavelength targets.

4. Experimental Sensitivities

A series of experiments was carried out to quantify the observed experimental sensitivity as well as for subsequent theory-to-experiment comparisons. Three types of targets were measured using an incoherent $\lambda = 450$ nm scatterfield optical microscope. We used an array of lines with 100 nm linewidth dimensions (± 5 nm) and 600 nm pitch, referred to as the “L100P600” target, that fill the FOV similar to those used in scatterometry. It is important to note that at $\lambda = 450$ nm, the L100P600 target scatters limited numbers of orders in addition to the zeroth-order specular reflection. This target is an essential test to validate the new Fourier domain normalization technique and its application to scattering, which results in a limited number of orders. Each type of target is fabricated using conventional lithography using a focus exposure matrix to provide a series of die with linewidth and sidewall profiles that vary on the nanometer scale.

The L100P600 targets are of particular interest as they contain only $m = -1, 0,$ and $+1$ orders at normal incidence, although the second order can be rocked in at high illumination angles. Figure 6 shows x and y polarization for a series of varying focus slices. Each panel at a given focus position shows eight profiles plotted together that correspond to eight different linewidth values, each acquired from a different die. For each polarization the figure shows 10 sets of plots with each set of

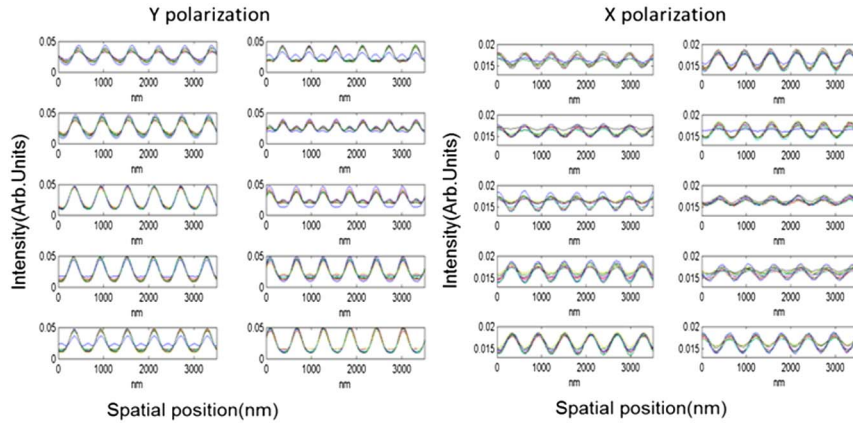


Fig. 6. Experimental focus-resolved L100P600 lines. The left side and right side data sets show profiles acquired from 400 nm above the substrate to 500 nm below in 100 nm increments.

profiles acquired at focus positions from 400 nm above the substrate to 500 nm below substrate in 100 nm increments.

Enlargements of the focus panels with best sensitivity from Fig. 6 are shown in Fig. 7, where the profiles from the eight die that were plotted together can be seen clearly. The σ_{repeat} values in the figure are the range of experimental repeatabilities for each data point scaled to the figures as labeled. The focus exposure matrix resulted in the eight die having a nominal variation in middle linewidth of 10 nm ranging from 115 to 125 nm and sidewall variations ranging from 5° to 8° from normal to the wafer, which resulted in curve differences on the order of 10^{-2} with each curve having a σ_{repeat} on the 10^{-3} scale, as shown in Fig. 7, thus demonstrating good sensitivity to the nanometer-scale changes in linewidth for the focus-resolved experiments.

Angle-resolved experiments for L100P600 show similar sensitivity. Figure 8 shows four groups of results with $y_{\text{scan}}, y_{\text{pol}}$; $y_{\text{scan}}, x_{\text{pol}}$; $x_{\text{scan}}, y_{\text{pol}}$; and $x_{\text{scan}}, x_{\text{pol}}$, with several panels showing profiles measured at various incident angles at the best focus position. Each panel at a given incident angle shows eight profiles plotted together that correspond to

eight different linewidth values, each again acquired at a different die.

In Fig. 9, the two graphs show sets of image profiles acquired at a given angle and at best focus, each showing eight profiles for the eight dies. The σ_{repeat} values are again the range of repeatabilities for each data point scaled to the figures as labeled, and the eight dies are the same as used for the L100P600 data above. Again, with curve differences on the order of 10^{-2} and each curve having a σ_{repeat} on the 10^{-3} scale, very good sensitivity to the linewidth variations is observed as a function of angle.

5. Parametric Fitting Results with Uncertainty Analysis

Accurate theory-to-experiment comparisons with minimal residuals are essential to develop quantitative modeling and an independent measurement capability. In this section we show a comparison of experimental data with theoretical simulations for two targets. For the L100P600 target, we define the model with four parameters: top width, middle width, bottom width, and height. Although this is not an isolated target as it fills the FOV, it provides an important demonstration and test of the modeling

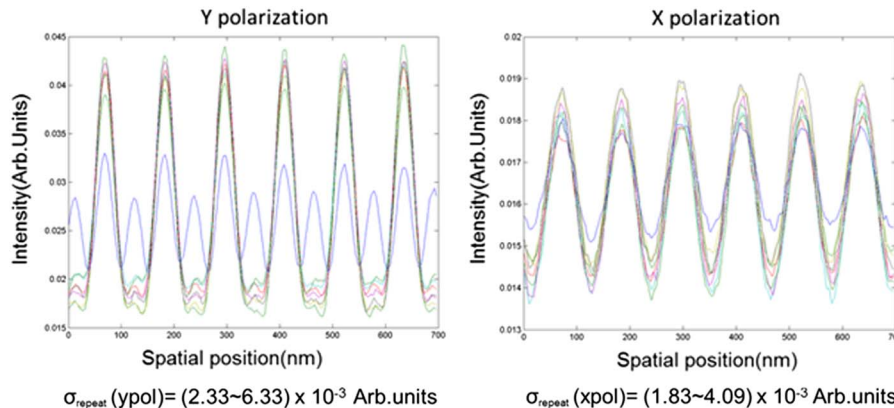


Fig. 7. Enlargement of one selected focus panel ($z = -100$ nm) from Fig. 6 to show the observed sensitivity among the eight dies.

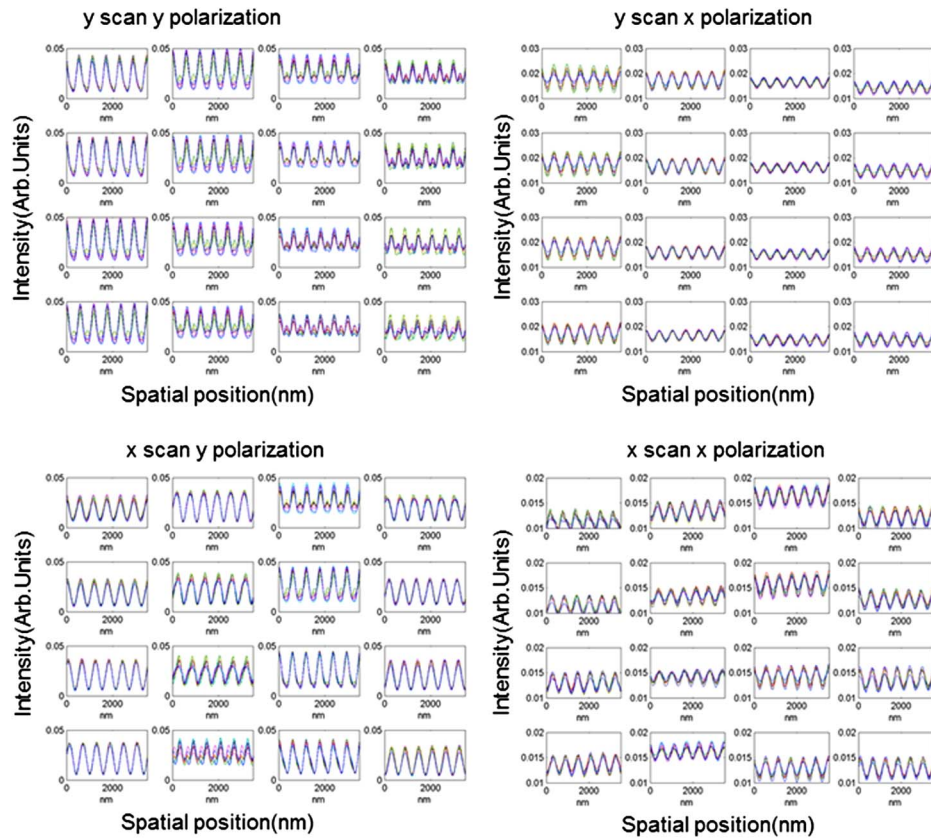
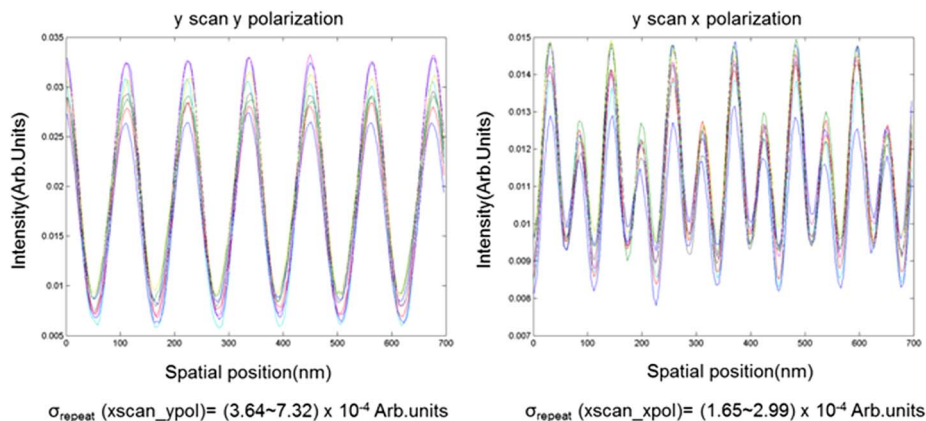


Fig. 8. Experimental angle-resolved L100P600 lines. From left side to right side data sets show profiles acquired at y_{scan}, y_{pol} ; y_{scan}, x_{pol} ; x_{scan}, y_{pol} ; and x_{scan}, x_{pol} .

and normalization method as it scatters well-defined scattering orders and there is substantial through-focus phase contrast and intensity variation. In Fig. 10 two polarizations are shown at normal incidence for four different focus positions with 100 nm increments. This uses the full Fourier normalization approach for the illumination path tool function and the collection path tool function applied to the scattered orders, as described in Section 2.

Another important and challenging test for this methodology is the measurement of a single Si edge with independently measured height of 222 nm and

sidewall angle of 3° (AFM reference measurement values), since an edge scatters a continuum of frequencies. The simulations are performed with a two-parameter geometrical model, the parameters being height and sidewall angle. We fit experimental data to normalized simulation data throughout the entire library, obtaining a best fit with a height of 228 nm and a sidewall angle of 2° . Figure 11 shows the entire fitting results through a $4 \mu\text{m}$ focus range, from $2 \mu\text{m}$ below the best focus to $2 \mu\text{m}$ above the best focus in 200 nm increments. In experiments, best focus is defined here using a focus metric (FM)



$$\sigma_{\text{repeat}}(x_{\text{scan}} y_{\text{pol}}) = (3.64 \sim 7.32) \times 10^{-4} \text{ Arb. units}$$

$$\sigma_{\text{repeat}}(x_{\text{scan}} x_{\text{pol}}) = (1.65 \sim 2.99) \times 10^{-4} \text{ Arb. units}$$

Fig. 9. Enlargement of angle-resolved experimental data for L100P600 lines from Fig. 8.

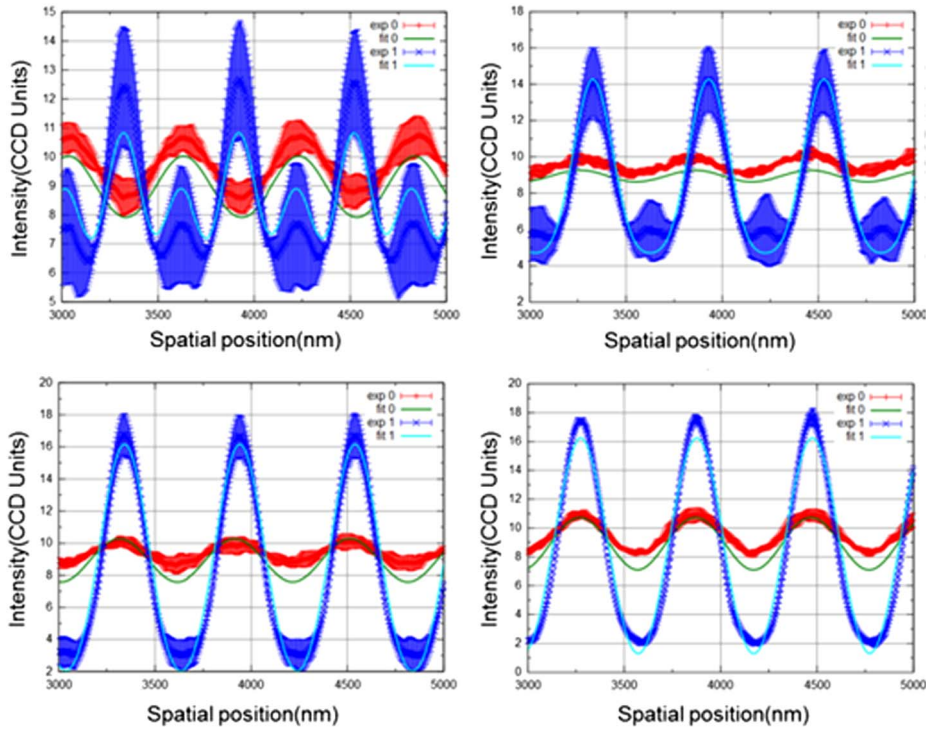


Fig. 10. Focus-resolved theory-to-experiment comparisons of the L100P600 target. The focus was varied in 100 nm increments between panels. Two different polarizations are shown in each graph.

algorithm separately for each polarization, which is defined by the integration of the gradient along the bottom peak of the profiles. The FM curves can show more than a 1 μm difference in best focus position between the x and y polarizations, as shown in Fig. 12. However, the x and y polarizations give the same best focus position in the simulated through focus image sets. This shift is most likely the result of the microscope beam splitter, which is fabricated from a material with inhomogeneous retardance. This is treated as a systematic error and addressed in the parametric fitting process separately for each

polarization; the focus position is independently floated for each polarization. This focus position difference between the two polarizations will be characterized in detail in future work.

The error bars shown in Fig. 11 only account for type A repeatability errors. Type B errors, such as systematic hardware errors, tool function error, and the phase error that can vary between different scattered frequencies, have not been fully considered in this example. Nevertheless, we observe consistent theory-to-experiment agreement throughout the entire 4 μm range. The fitting results for x polarization

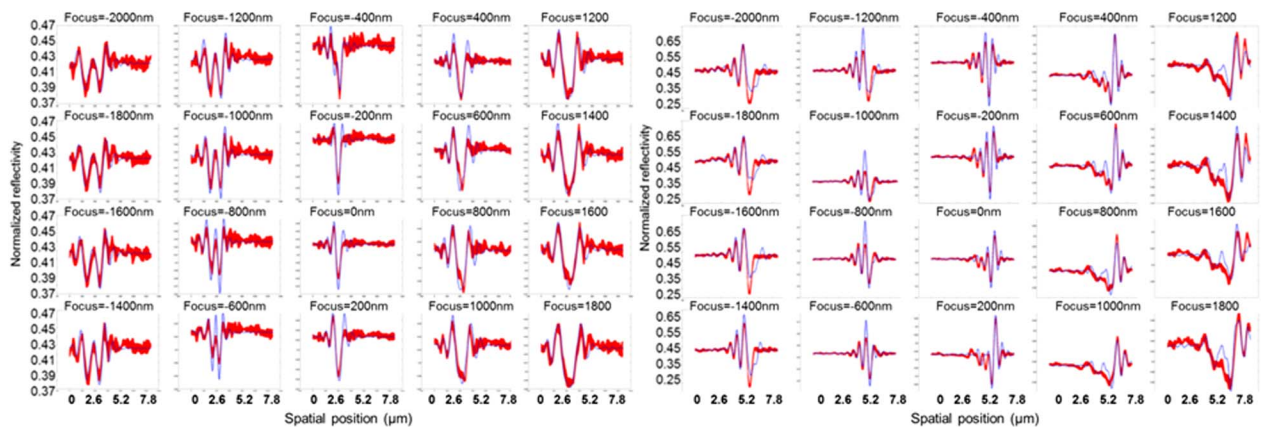


Fig. 11. Focus-resolved theory-to-experiment comparisons of the Si single edge target. The focus was varied in 200 nm increments between panels, and 20 panels in total shows focus positions vary from 2 μm below best focus to 2 μm above best focus. Left is for x polarization, and right is for y polarization.

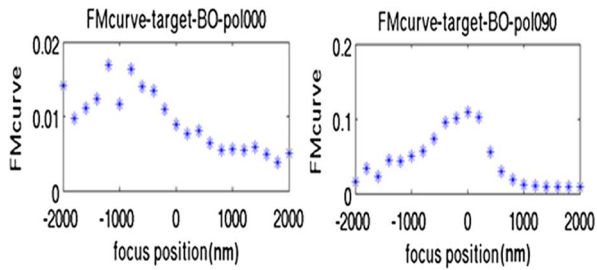


Fig. 12. FM curves for both x polarization (left) and y polarization (right).

are shown in the left group of figures, and the y polarization data are shown in the right group of figures. Note that they are plotted on different scales, as x polarization profiles vary over a smaller normalized reflectivity range than those for the y polarization. Although the change is over a smaller range, the x polarization shows more sensitivity to changes in linewidth, based on the significant change in the profile shapes.

In Fig. 13, we selected eight images at different focus positions from Fig. 12 and increased the error bars to estimate the type B errors [15], such as aperture size uncertainty, aperture position uncertainty, intensity uncertainty for focus position increment error, phase error from image system mapped into intensity uncertainty, tool function repeatability error mapped into simulation data normalization, errors from the geometric model, etc. After the regression analysis, we calculate the parametric uncertainties for height and sidewall angle as 0.08 nm and 0.03° . These uncertainty values are quite small, which is in part the direct result of virtually no correlation between the two geometric parameters, step height and sidewall angle. The excellent sensitivity that the experimental data show through the range of focus also contributes to this extremely small uncertainty. Although further error analysis is needed to refine the error bars and obtain more realistic expanded uncertainties, the experimental data and

the simulation studies demonstrate that the fundamental basis for decreased uncertainties using these techniques is valid.

6. Conclusion

Using accurate optical tool characterization and frequency domain normalization, a path to quantitative modeling was demonstrated for targets with a scattered electromagnetic field containing multiple spatial frequencies. Both the modeling and experimental data demonstrate that nanometer-scale measurements can be achieved using angle-resolved or focus-resolved scatterfield microscopy. Sensitivity was demonstrated in measurements of grating targets that scatter limited numbers of orders, as well as isolated edge targets that scatter a broad range of higher-order diffracted light. A sophisticated approach must be applied in the Fourier domain that corrects optical path errors in both the illumination and collection paths throughout the angular spectrum as a function of polarization. With this approach, both the L100P600 and single Si edge targets show consistent theory-to-experiment fitting results throughout a wide focal range. By concatenating image-based profiles from several focus heights into a single data string and performing a rigorous regression analysis against a library of physics-based simulations, we can potentially decrease parametric uncertainty to the subnanometer scale. Analyzing type A and estimating type B uncertainty components, subnanometer parametric uncertainties were obtained. These results suggest a potential new basis for the quantitative measurement of targets having finite, sub-FOV overall dimensions composed of deep subwavelength sized features.

The authors thank SEMATECH for wafer fabrication and measurement support. The authors thank Thomas Germer for providing a 2-D RCWA code and are indebted to Nien-Fan Zhang for research in developing the regression analysis and Bayesian statistical methods.

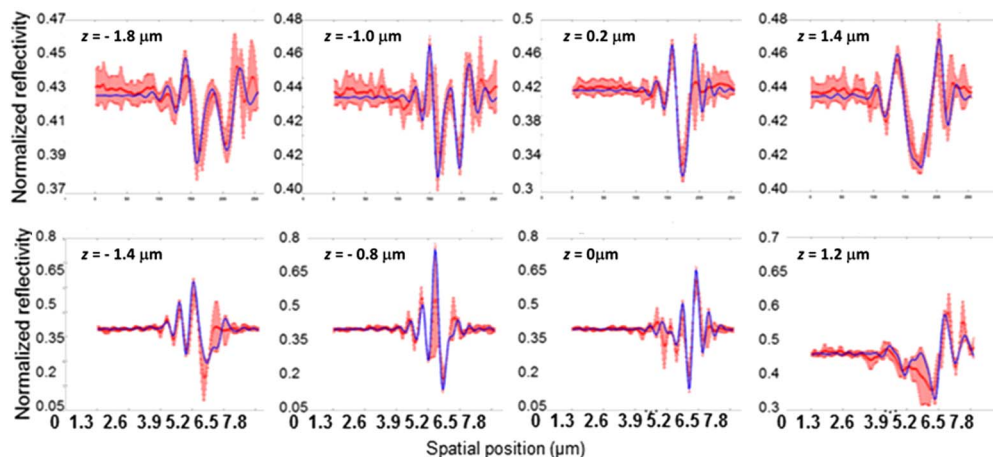


Fig. 13. Selected examples at various focus position from the fitting results shown in Fig. 11 with increased error bars.

References

1. R. M. Silver, B. Barnes, R. Attota, J. Jun, M. Stocker, E. Marx, and H. Patrick, "Scatterfield microscopy to extend the limits of image-based optical metrology," *Appl. Opt.* **46**, 4248–4257 (2007).
2. H. Patrick, R. Attota, B. Barnes, T. Germer, R. G. Dixon, M. Stocker, R. M. Silver, and M. Bishop, "Optical critical dimension measurement of silicon grating targets using back focal plane scatterfield microscopy," *J. Microlithogr., Microfabr., Microsyst.* **7**, 0137011 (2007).
3. B. M. Barnes, L. P. Howard, J. Jun, P. Lipscomb, and R. M. Silver, "Zero-order imaging of device-sized overlay targets using scatterfield microscopy," *Proc. SPIE* **6518**, 65180F (2007).
4. R. M. Silver, N. F. Zhang, B. Barnes, H. Zhou, A. Heckert, R. Dixon, T. Germer, and B. Bunday, "Improving optical measurement accuracy using multi-technique nested uncertainties," *Proc. SPIE* **7272**, 727202 (2009).
5. R. M. Silver, R. Attota, M. Stocker, M. Bishop, J. Jun, E. Marx, M. Davidson, and R. Larrabee, "The limits of image-based optical metrology," *Proc. SPIE* **6152**, 61520Z (2006).
6. R. M. Silver, R. Attota, M. Stocker, M. Bishop, L. Howard, T. Germer, E. Marx, M. Davidson, and R. Larrabee, "High-resolution optical metrology," *Proc. SPIE* **5752**, 67–79 (2005).
7. Y. J. Sohn, B. M. Barnes, L. Howard, R. M. Silver, R. Attota, and M. T. Stocker, "Koehler illumination in high-resolution optical metrology," *Proc. SPIE* **6152**, 61523S (2006).
8. B. M. Barnes, R. Attota, R. Quintanilha, Y. J. Sohn, and R. M. Silver, "Characterizing a scatterfield optical platform for semiconductor metrology," *Meas. Sci. Technol.* **22**, 024003 (2011).
9. R. M. Silver, N. F. Zhang, B. Barnes, H. Zhou, J. Qin, and R. Dixon, "Nested uncertainties to improve measurement accuracy," *Proc. SPIE* **7971**, 797116 (2011).
10. N. F. Zhang, R. M. Silver, H. Zhou, and B. M. Barnes, "Improving optical measurement uncertainty with combined multitool metrology using a Bayesian approach," *Appl. Opt.* **51**, 6196–6206 (2012).
11. C. R. Rao and H. Toutenburg, *Linear Models: Least Squares and Alternatives* (Springer, 1995).
12. D. M. Bates and D. G. Watts, *Nonlinear Regression Analysis and Its Applications* (Wiley, 1998).
13. M. G. Moharam, D. A. Pommet, E. B. Grann, and T. K. Gaylord, "Stable implementation of the rigorous coupled wave analysis for surface-relief gratings: enhanced transmittance matrix approach," *J. Opt. Soc. Am. A* **12**, 1077–1086 (1995).
14. R. M. Silver, J. Qin, B. M. Barnes, H. Zhou, R. Dixon, and F. Goasmat, "Phase sensitive parametric optical metrology: exploring the limits of three-dimensional optical metrology," *Proc. SPIE* **8324**, 83240N (2012).
15. US Guide to the Uncertainty of Measurement, American National Standards Institute (1997).